Medical Image Segmentation by Combining Graph Cuts and Oriented Active Appearance Models

Xinjian Chen, Jayaram K. Udupa, Ulas Bagci, Ying Zhuge, and Jianhua Yao

***Abstract*—In this paper, we propose a novel method based on a strategic combination of the active appearance model (AAM), live wire (LW), and graph cuts (GCs) for abdominal 3-D organ segmentation. The proposed method consists of three main parts: model building, object recognition, and delineation. In the model building part, we construct the AAM and train the LW cost function and GC parameters. In the recognition part, a novel algorithm is proposed for improving the conventional AAM matching method, which effectively combines the AAM and LW methods, resulting in the oriented AAM (OAAM). A multiobject strategy is utilized to help in object initialization. We employ a pseudo-3-D initialization strategy and segment the organs slice by slice via a multiobject OAAM method. For the object delineation part, a 3-D shape-constrained GC method is proposed. The object shape generated from the initialization step is integrated into the GC cost computation, and an iterative GC–OAAM method is used for object delineation. The proposed method was tested in segmenting the liver, kidneys, and spleen on a clinical CT data set and also on the MICCAI 2007 Grand Challenge liver data set. The results show the following: 1) The overall segmentation accuracy of true positive volume fraction TPVF $> 94.3\%$ and false positive volume fraction FPVF $< 0.2\%$ can be achieved; 2) the initialization performance can be improved by combining the AAM and LW; 3) the multiobject strategy greatly facilitates initialization; 4) compared with the traditional 3-D AAM method, the pseudo-3-D OAAM method achieves comparable performance while running 12 times faster; and 5) the performance of the proposed method is comparable to state-of-the-art liver segmentation algorithm. The executable version of the 3-D shape-constrained GC method with a user interface can be downloaded from http://xinjianchen.wordpress.com/research/.**

***Index Terms*—Active appearance model (AAM), graph cut (GC), live wire (LW), object segmentation.**

I. Introduction

IMAGE segmentation is a fundamental and challenging problem in computer vision and medical image analysis. In spite of several decades of research and many key advances, several challenges still remain in this area. Efficient, robust, and automatic segmentation of anatomy on radiological images is one such challenge.

The image segmentation methods may be classified into several types: image-based [1]–[12], model-based [13]–[29], and hybrid methods [30]–[38]. Purely image-based methods perform segmentation based only on information available in the image; these include thresholding, region growing [1], morphological operations [2], active contours [3], [4], [22], level sets [5], live wire (LW) [6], watershed [7], fuzzy connectedness [8], [9], and graph cuts (GCs) [10], [11], [46]. These methods perform well on high-quality images. However, the results are not as good when the image quality is inferior or boundary information is missing. In recent years, there has been an increasing interest in model-based segmentation methods. One advantage of these methods is that, even when some object information is missing, such gaps can be filled by drawing upon the prior information present in the model. The model-based methods employ object population shape and appearance priors such as atlases [13]–[17], [23], [24], statistical active shape modes [18]–[20], [25], and statistical active appearance models (AAMs) [21], [26], [27]. The MICCAI 2007 "Grand Challenge" workshop [28] organized a competition for liver segmentation, which attracted much attention. In that competition, the three best-rated approaches [28], [29] were all based on statistical shape models with some form of additional deformation. Such hybrid approaches are rightfully attracting a great deal of attention at present. The synergy that exists between these two approaches, i.e., purely image-based and model-based strategies, is clearly emerging in the segmentation field. As such, hybrid methods that form a combination of two or more approaches are emerging as powerful segmentation tools [30]–[38], where their superior performances and robustness over each of the components are beginning to be well demonstrated.

Most of the image-based [1], [4], model-based [14]–[18], [20]–[24], [29], and even hybrid segmentation [38] techniques are often tailored for specific body regions (brain, abdomen, etc.) and different image modalities (CT, MRI, etc.). However, it is desirable to generalize image segmentation methodologies for any (or most) body regions and different image modalities and protocols. Furthermore, it is desirable for an image segmentation algorithm not to heavily depend upon the characteristics of fixed shape families and different image modalities. While perhaps some of the above techniques can be generalized in this spirit, few methods have demonstrated to work in this general setting.

In this paper, we propose a general method to segment body organs by effectively combining the LW, AAM, and GC methods to construct a new technique, which is named

Manuscript received December 27, 2010; revised May 10, 2011, October 03, 2011, and January 04, 2012; accepted January 09, 2012. Date of publication January 31, 2012; date of current version March 21, 2012. This work was supported in part by the Intramural Research Program of the Clinical Center, NIH. The associate editor coordinating the review of this manuscript and approving it for publication was Prof. Margaret Cheney.

X. Chen, U. Bagci, and J. Yao are with the Department of Radiology and Imaging Sciences, Clinical Center, National Institute of Health, Bethesda, MD 20814 USA (e-mail: myfuturejian@gmail.com; bagciu@mail.nih.gov; jyao@mail.nih.gov).

J. K. Udupa is with the Medical Image Processing Group, Department of Radiology, University of Pennsylvania, Philadelphia, PA 19104 USA (e-mail: jay@mail.med.upenn.edu).

Y. Zhuge is with the Radiation Oncology Branch, National Cancer Institute, National Institute of Health, Bethesda, MD 20814 USA (e-mail: zhugey@mail.nih.gov).

Color versions of one or more of the figures in this paper are available online at http://ieeexplore.ieee.org.

Digital Object Identifier 10.1109/TIP.2012.2186306

TABLE I
DESCRIPTION OF SOME OF THE ABBREVIATIONS USED IN THE PAPER

bel	Boundary Element	*MOAAM*	Multi-object Oriented Active Appearance Model
GC	Graph Cut	*GC-OAAM*	Graph Cut Oriented Active Appearance Model
LW	Live wire	*IGC-OAAM*	Iterative Graph Cut Oriented Active Appearance Model
AAM	Active Appearance Model	FPVF	False Positive Volume Fraction
OAAM	Oriented Active Appearance Model	TPVF	True Positive Volume Fraction
MAAM	Multi-object Active Appearance Model		

GC–OAAM. LW is a user-steered 2-D segmentation method in which the user provides recognition help and in which the algorithm performs optimal delineation. The main limitation of LW stems from the recognition process, wherein the anchor points are to be selected on the boundary by a human operator. AAM methods use landmarks to represent shape and appearance and use principal component analysis to capture the major modes of variation in shape and appearance observed in the training data sets. However, the specific shape and appearance information on the object in a given image is difficult to account for in these methods. GC methods have the ability to compute globally optimal solutions (in the two-label case) and can enforce piecewise smoothness. However, they are interactive methods, requiring labeling of the source and sink seeds by a human operator. In this paper, our aim is to combine the complementary strengths of these individual methods to arrive at a more powerful hybrid strategy to overcome the weakness of the component methods.

Several existing approaches embody hybrid integration in the above spirit. For instance, Besbes *et al.* [12] proposed a segmentation method based on Markov random fields, which combined shape priors and regional statistics. However, this method did not perform segmentation at the pixel level. Freedman and Zhang [33] incorporated a shape template into the GC formulation as a distance function. However, it relied crucially on user input. As another example, Ayvaci and Freedman [34] proposed a joint registration–segmentation method, avoiding the user interaction and resolving the problem of template registration. However, this method required proper registration of the shape template for an accurate segmentation. This is not only a difficult task but also computationally expensive. Kumar et al. [35] used a Markov random field representation where the latent shape model variables were integrated via expectation–maximization. While shape information was utilized in a principled Bayesian manner, this approach was computationally intensive because a separate energy minimization is required. Malcolm et al. [36] imposed a shape prior model on the terminal edges and iteratively performed GC optimization starting from an initial contour. This method also relied on user input. More recently, Vu and Manjunath [37] have proposed a method integrating shape prior with GC for multiobject segmentation. The proposed prior shape energy is based on a shape distance function similar to that used in level-set approaches. However, the prior shape is kept fixed; therefore, the generalizability of the method is questionable. Most of the methods aforementioned operate on 2-D images.

Our proposed segmentation methodology is different from the methods reported in the literature by the following considerations: 1) The strategy proposed in this paper is a 3-D technique; 2) it does not need registration of shapes, unlike the methods previously summarized; and 3) to the best of our knowledge, GC–OAMM is the only method that simultaneously combines the rich statistical shape and appearance information in the AAM as well as the effective boundary-oriented delineation capability of LW and the globally optimal delineation capability of the GC method.

In the rest of this paper, in Section II, we elaborate the complete methodology of the delineation algorithm. In Section III, we describe an evaluation of this method in terms of its accuracy and efficiency. In Section IV, we summarize our contributions and conclusions. The common terms and abbreviations used in the manuscript are listed in Table I.

II. GC–OAMM APPROACH

A. Overview of the Approach

The proposed method consists of two phases: training and segmentation. Fig. 1 presents an overview of the proposed method. In the training phase, an AAM is constructed, and the LW boundary cost function and GC parameters are estimated. The segmentation phase consists of two main steps: recognition or initialization and delineation. In the recognition step, a pseudo-3-D initialization strategy is employed in which the pose of the organs is estimated slice by slice via a multiobject OAAM (MOAAM) method. A further refinement may be needed to adjust the initialization of improperly initialized slices. The pseudo-3-D initialization strategy is motivated by two reasons. First, 3-D initialization is difficult and has computational drawbacks; the proposed method is much faster. Second, combining the AAM and LW in a 3-D manner is challenging. Indeed, the pseudo-3-D method offers fast initialization, and its performance is comparable to the fully 3-D AAM initialization method. Finally, for the delineation part, the object shape information generated from the initialization step is integrated into the GC cost computation. The details of each step are given in the following subsections.

B. Model Building and Parameter Training

Before building the model, the top and bottom slices of each organ are first manually identified. Then, linear interpolation is applied to generate the same number of slices for the organ in

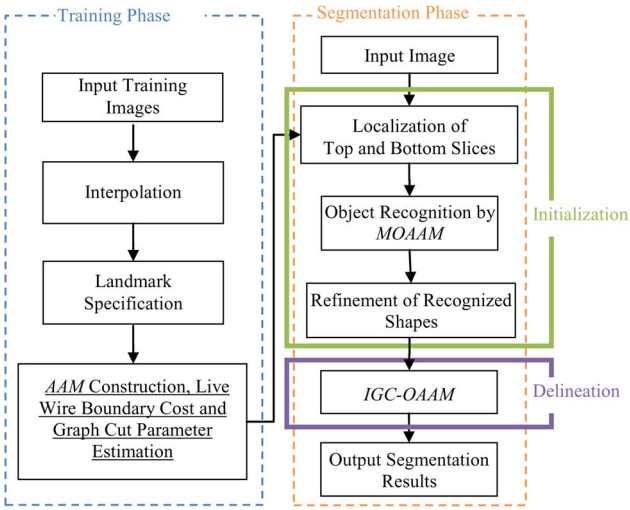

Fig. 1. Flowchart of the proposed GC–OAMM system.

every training image. This is for establishing anatomical correspondences. 2-D OAAM models are then constructed for each slice level from the images in the training set. The LW cost function and GC parameters are also estimated in this stage.

Landmark Specification: We represent a 3-D shape as a stack of 2-D contours and manually annotate the 3-D shape slice by slice. Although semiautomatic or automatic methods are also available for annotating organs because of its simplicity, generality, and efficiency, manual landmarking is still in use in clinical research. Therefore, we use manual landmarking to annotate organs' shape. In manual landmarking, trained operators identify prominent landmarks on each shape visually on displayed slices.

We assessed a semiautomatic landmarking method, which is called equal-space landmarking [49], to show that there is a strong correlation between the shapes encoded by the manual and semiautomated landmarking methods. Since we treat shape as an infinite point set in principle, it can be assumed that the shape of an object is captured by a finite subset of a sufficient number of its points. Therefore, different numbers of landmarks are used for different objects based on their size. Since there is a vast amount of literature on the analysis of effects of distribution of landmarks on model building and segmentation results, we avoid repeating these experiments, but we validate manual landmarking by the equal-space labeling method.

AAM Construction: Once the landmarks are specified, the standard AAM method [26], [27] is used for constructing the model. The model includes both shape and texture information. Suppose M_j represents the AAM model for slice level j and the number of slice levels is n, then the complete model M can be represented as $M = (M_1, M_2, \ldots, M_n)$.

Although we employ a pseudo-3-D initialization strategy, we also build the fully 3-D AAM, which is denoted as $M_{3\mathrm{D}}$, using the method in [42]. This 3-D model is used only for providing the delineation constraints, as explained later.

LW Cost Function and GC Parameter Training: Similar to the oriented active shape model method [30], an oriented boundary cost function is devised for each organ included in the model M as per the LW method [6]. Following the original terminology and notation in [6], we define a *boundary element*

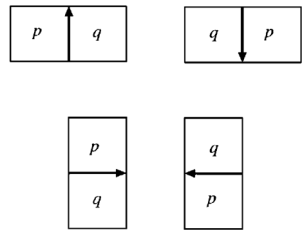

Fig. 2. Bel is an oriented pixel edge. The four possible types of bels in a scene are shown. The inside of the boundary is to the left of the bel, and the outside is to the right.

(bel) as an oriented edge between two pixels with values 1 and 0. For a given image slice I, a bel will be represented as an ordered pair (p, q) of four adjacent pixels, where p is inside the object (pixel value 1) and q is outside (pixel value 0), as illustrated in Fig. 2. We think of every pixel edge of I as constituting two potential bels (p, q) and (q, p) and possibly assign different cost values to them. To every bel of I, we assign a set of features depending on the orientation (p, q) or (q, p). The features assigned to each bel are intended to express the likelihood of the bel belonging to the boundary of a particular object of interest. In our particular case, the cost $c(l)$ associated with bel l is a linear combination of the costs assigned to its features

$$c(l) = \frac{\sum_{i=1}^{nf} w_i c_f\left(f_i(l)\right)}{\sum_{i=1}^{nf} w_i} \tag{1}$$

where nf is the number of features, w_i is a positive constant indicating the emphasis given to feature f_i, and c_f is the function to convert feature values $f_i(l)$ at l to cost values $c_f(f_i(l))$. In LW [6], f_i may represent features such as intensity on the immediate interior of the boundary, intensity on the immediate exterior of the boundary, and gradient magnitude at the center of the bel. Depending on the intensity characteristics of the object of interest, different f_i may be combined. As suggested in [6], c_f is chosen as an inverted Gaussian function, and all selected features are combined with uniform weights w_i. We utilize the feature of LW to define the best oriented path between any two landmark points (x_k and x_{k+1}) as a sequence of bels with minimum total cost, i.e.,

$$\kappa(x_k, x_{k+1}) = \sum_{i=1}^{h} c(l_i) \tag{2}$$

where h represents the number of bels in the best oriented path $\langle l_1, l_2, \ldots, l_h \rangle$. The total cost structure $\boldsymbol{\kappa}(\mathbf{x})$ associated with all the landmarks may now be defined as

$$\boldsymbol{\kappa}(\mathbf{x}) = \sum_{k=1}^{m} \boldsymbol{\kappa}(X_k, X_{k+1}) \tag{3}$$

where m is the number of landmarks for the object of interest, and we assume that $\mathbf{x}_{m+1} = \mathbf{x}_1$ (closed contour). In other words, $\boldsymbol{\kappa}(\mathbf{x})$ is the sum of the costs associated with the best

oriented paths between all m pairs of successive landmarks of shape instance $\mathbf{x}$. The parameters of $\boldsymbol{\kappa}(\mathbf{x})$ for each object shape $\mathbf{x}$ are estimated automatically, as described in [6], by using the training images.

For the sake of continuity, the description of how the parameters of GC are estimated is given in Section II-F, where the modified GC algorithm is described.

C. Recognition/Initialization

The initialization step plays a key role in our method, which provides the shape constraints to the later GC delineation step and makes it fully automatic. The proposed initialization method includes three main steps. First, a slice localization method is applied to detect the top and bottom slices of the organ. Next a linear interpolation is applied to generate the same number of slices for the given image of a subject, as in the model. Then, the organ is recognized slice by slice via the OAAM method. A multiobject strategy [43] is utilized to help with object recognition. Our experiments indicate that the recognition performance with multiple organs in the model is much better than with a single organ due to the constraints coming from multiple organs. Even if just one organ is to be segmented, other organs can be included in the model to provide context and constraints. Finally, a refinement method is applied to the initialization result. These three steps are described in the following in detail.

D. Localization of Top and Bottom Slices

There have been several recent works related to slice localization. Haas et al. [38] introduced an approach to creating a navigation table using eight landmarks, which were detected in various ways. Seifert et al. [19] proposed a method to detect invariant slices and single-point landmarks in full-body scans by using a probabilistic boosting tree and Haar features. Emrich et al. [39] proposed a CT slice localization method via k-nearest-neighbor-instance-based regression. The aim of slice localization in our approach is to locate the top and bottom slices of the organ. Since the model is already trained for each organ slice, we can use the model for slice localization. The proposed method is based on the similarity of the slice to the OAAM model.

For the localization of a top slice in a given image, the top-slice model is applied to each slice in the image using the recognition method detailed in Section II-E. Then, the slice corresponding to maximal similarity (minimal distance) is taken as the top slice of the organ. Fig. 3 shows the distance value [computed from (5)] for the localization of top slice in a patient abdominal CT image. The minimum corresponds to the top slice of the left kidney. For the detection of bottom slice, a similar method is used.

E. Object Recognition

The proposed object recognition method is based on the AAM. The conventional AAM matching method for object recognition is based on the RMS difference between the appearance model instance and the target image. Such a strategy is better suited for matching appearances than for the detailed segmentation of target images [see Fig. 4(b)]. This is because

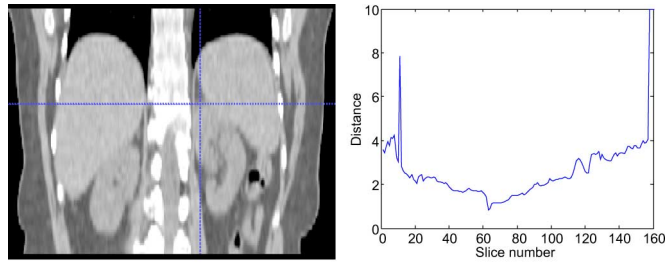

Fig. 3. Illustration of top-slice recognition. (a) Coronal view of the abdominal region. Cross point represents the top slice of the left kidney. (b) The distance values of each slice to the top-slice model for the left kidney.

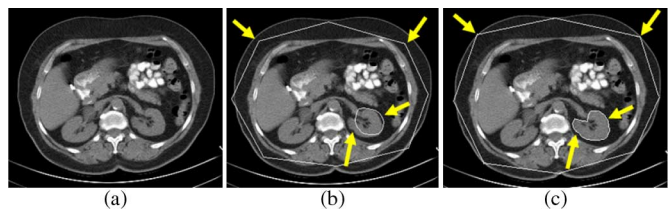

Fig. 4. Comparison of conventional AAM and OAAM segmentation. (a) Original image. (b) Conventional AAM segmentation showing a good appearance fit but poor boundary detection accuracy (arrows). (c) OAAM result shows substantial improvement in boundary location (arrows).

the AAM is optimized on global appearance, and is thus less sensitive to local structures and boundary information. Conversely, the LW delineates the boundary very well [6]; however, it needs good initialization of landmarks and is an interactive method. Here, we integrate the AAM with the LW method (termed OAAM) to combine their complementary strengths. That is, the AAM provides the landmarks to the LW, and in return, LW improves the shape model of the AAM. The LW is fully integrated with AAM in two aspects: 1) LW is used to refine the shape model in AAM; and 2) the LW boundary cost is integrated into cost computation during the AAM optimization method. Fig. 4(c) shows the proposed OAAM segmentation result; compared with conventional AAM method [see Fig. 4(b)], the boundary delineation is much improved.

Refinement of the Shape Model in the AAM by LW: First, the conventional AAM searching method is performed once to obtain a rough placement of the model. Then, the following method is applied to refine the shape model in the AAM. The shape is extracted from the shape model of the AAM, and then the landmarks are updated based on LW using only the shape model and the pose parameters (i.e., translation, rotation, and scale) (following [30]), as shown in Fig. 5. Subsequently, the refined shape model is transformed back into the AAM. At the same time, AAM refinement is applied to the image yielding its own set of coefficients for shape and pose.

Algorithm 1: Refine AAM shape model based on LW

Input: The shape model $\mathbf{x}$.

Output: Updated shape model $\mathbf{x}'$ and new affine transformation t'.

Begin

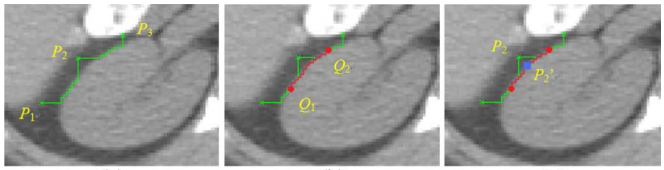

Fig. 5. Illustration of how to update the position of the landmarks. (a) P_1, P_2, and P_3 are three landmarks from AAM shape results. (b) The middle point Q_1 of the LW segment between P_1 and P_2, and similarly Q_2 for P_2 and P_3 are generated. (c) Landmark P_2 is moved to the closest point P_2' on the LW segment from Q_1 to Q_2.

For each triple P_1, P_2, and P_3 of successive landmarks on $\mathbf{x}$

1) Perform LW delineation from P_1 to P_2 and P_2 to P_3.
2) Find the middle points Q_1 and Q_2 in the LW segments generated from P_1 to P_2 and from P_2 to P_3, respectively.
3) Perform LW delineation from Q_1 to Q_2.
4) Find the point P_2' on the LW segment from Q_1 to Q_2 closest to P_2, and update P_2 to P_2'.

EndFor

5) Transform the obtained shape $\mathbf{x}_r$ into a new shape model instance x' by aligning $\mathbf{x}_r$ to the mean shape $\bar{\mathbf{x}}$ which yielding the new affine transformation t'.

Apply the model constraints to the new shape model x' so that the new shape is within the allowed shape space.

End

OAAM Optimization: In the conventional AAM matching method, the optimization is based only on the difference between the appearance model instance and the target image. The boundary cost is not taken into consideration. By combining the boundary cost, the performance of AAM matching can be considerably improved. In the proposed method, the LW technique is integrated into the cost computation during the optimization process. Suppose that the current estimate of the AAM model parameters is b, which includes both shape and texture information, as follows:

$$b = Q^T \begin{pmatrix} b_s \\ b_g \end{pmatrix} \tag{4}$$

where Q is a matrix describing the modes of shape and appearance variation derived from the training set, b_s is the shape model parameters, and b_g is the appearance model parameters. Combined with the above shape model refinement method, our optimization method is as follows.

Algorithm 2: OAAM Optimization

Input: Model-parameter vector b, pose vector t, texture vector u, weight parameters $\alpha_1 = \alpha_2 = 0.5$.

Output: Updated model-parameter vector b, t, and u.

Begin

1. Extract shape parameters b_s from b, refine b_s using Algorithm 1, get the updated shape model parameters b_s' and pose t', and update b by $b = Q^T \begin{pmatrix} b_s' \\ b_g \end{pmatrix}$.
2. Based on the updated b and t', resample the image intensity as g_{im}' and compute the texture model frame using $g_s' = T_u^{-1}(g_{\text{im}}')$.
3. Evaluate the errors
   a. Texture error $E_{\text{aam}} = |r(\phi)|^2$, where $\phi^T = (b^T | t'^T | u^T)$ and $r(\phi) = g_s' - g_{\text{im}}'$.
   b. Total error by combining E_{aam} and LW cost along the shape boundary E_{lw}, i.e.,
   $$E_{\text{total}} = \alpha_1 \cdot E_{\text{aam}} + \alpha_2 \cdot E_{lw}. \tag{5}$$
4. Compute the predicted displacements $\delta_\phi = -Rr(\phi)$, where $R = ((\partial r^T/\partial\phi)(\partial r/\partial\phi))^{-1}(\partial r^T/\partial\phi)$.
5. Set $k = 1$.
6. Update the parameters $\phi \leftarrow \phi + k\delta_\phi$.
7. Based on the new parameters ϕ, repeat steps 1–3, and get the new error E_{total}'.
8. If $E_{\text{total}}' < E_{\text{total}}$, then accept the new parameters, and go to step 9.
   Else, try $k = 0.5, 0.25$, etc., and go to step 6.
9. Repeat staring with step 1 until no improvement is made to the total error.

End

During initialization, we employ a multiresolution strategy, in which we start at a coarse resolution and iterate to convergence at each level before starting the next level. This strategy is more efficient than searching at a single resolution and can lead to a convergence to the correct solution even when the model position is away from the real object(s). One may wonder if it is ever possible for $E_{\text{total}}' < E_{\text{total}}$ to be true. Since the total error function is a linear combination of the nonlinear functions of LW and AAM costs, one may expect a discrepancy between these error functions because they operate in different domains: shape and image space. Therefore, an increase in AAM costs may not be exactly overcome by the cost of LW, leading to $E' < E$ becoming false. Another important factor that affects this condition is due to high variation of E_{aam} error stemming from large texture nonuniformity, although the LW cost becomes stable over the iterations. Getting trapped in local minima is another well-known problem of conventional AAM optimization. Hence, changing the ratio of the contributing errors into the total cost may overcome such difficulties, although this problem is difficult to solve in a fail-safe manner.

Refinement of the 3-D Recognized Shapes: After objects are recognized in all slices, the recognized shapes are stacked together to form 3-D objects. We observed from experiments that, sometimes, the initialization result for one slice is far away from the results for its neighboring slices. This signals failure of recognition for this slice. We found that at most two slices failed in recognition in this sense in all of our experiments (in 80 cases, nonfailed: 71; 1 slice failed: 7; two slices failed: 2). When failure occurs, we interpolate the new shape from the shapes in neighboring slices. The following method is applied to improve the recognized shape results.

Algorithm 3: Refinement of the 3-D recognized shape

Input: Slices $1 \le j \le n$, weights $\eta_1 = 0.5$, $\eta_2 = 0.25$ and $\eta_3 = 0.25$, and the threshold of reliability thre_j (estimated from training data).

Output: Refined 3-D shape.

Begin

For $j = 1 : n$

1. Compute the distance between the centroids of the shapes in slices $j-1$ and $j+1$ as d_{j-1} and d_{j+1}
2. Compute the total reliability for slice j as

$$\mathrm{rel}_j = \eta_1 \cdot \left(\frac{e_{\max} - e}{e_{\max}}\right) + \eta_2 \cdot \exp\left(-\frac{(d_{j-1} - \mu(d_{j-1}))^2}{2 \cdot \mathrm{var}(d_{j-1})}\right) + \eta_3 \cdot \exp\left(-\frac{(d_{j+1} - \mu(d_{j+1}))^2}{2 \cdot \mathrm{var}(d_{j+1})}\right).$$

3. If $\mathrm{rel}_j < thre_j$, then estimate the shape in slice j via interpolation from the neighboring slices.

EndFor

End

Here, $\mu(d_{j-1})$, $\mathrm{var}(d_{j-1})$, $\mu(d_{j+1})$, and $\mathrm{var}(d_{j+1})$ are the mean and variance of d_{j-1} and d_{j+1}, respectively, which are estimated from training images during the model building process. e and $e_{\max}$ represent current and maximum slice localization errors, respectively. It is worthy to notice that, for the first slice and the last slice, only one neighbor slice is used for the given algorithm.

F. Delineation

The purpose of this step is to finally precisely delineate the shapes recognized in the previous step. We propose an iterative algorithm combining GC and OAAM (named IGC–OAMM) method for the organ's delineation. The IGC–OAMM algorithm effectively integrates the shape information with the globally optimal 3-D delineation capability of the GC method.

Shape-Integrated GC: GC segmentation can be formulated as an energy minimization problem such that, for a set of pixels P and a set of labels L, the goal is to find a labeling $f\colon P \to L$ that minimizes the energy function $\mathrm{En}(f)$ as follows:

$$\mathrm{En}(f) = \sum_{p \in P} R_p(f_p) + \sum_{p \in P, q \in N_p} B_{p,q}(f_p, f_q) \tag{6}$$

where N_p is the set of pixels in the neighborhood of p, $R_p(f_p)$ is the cost of assigning label $f_p \in L$ to p, and $B_{p,q}(f_p, f_q)$ is the cost of assigning labels $f_p, f_q \in L$ to p and q. In two-class labeling, $L = \{0, 1\}$, the problem can be solved efficiently with GCs in polynomial time when $B_{p,q}$ is a submodular function, i.e., $B_{p,q}(0,0) + B_{p,q}(1,1) \leq B_{p,q}(0,1) + B_{p,q}(1,0)$ [11].

In our framework, the unary cost $R_p(f_p)$ is the sum of a data penalty $D_p(f_p)$ term and a shape penalty $S_p(f_p)$ term. The data term is defined based on image intensity and can be considered as a log likelihood of the image intensity for the target object. The shape prior term is independent of image information, and the boundary term is based on the gradient of the image intensity.

The proposed shape-integrated energy function is defined as follows:

$$\mathrm{En}(f) = \sum_{p \in P} (\alpha \cdot D_p(f_p) + \beta \cdot S_p(f_p)) + \sum_{p \in P, q \in N_p} \gamma \cdot B_{p,q}(f_p, f_q) \tag{7}$$

where α, β, and γ are the weights for the data term, shape term S_p, and the boundary term, respectively, satisfying $\alpha + \beta + \gamma = 1$. These components are defined as follows:

$$D_p(f_p) = \begin{cases} -\ln P(I_p|O), & \text{if } f_p = \text{object label} \\ -\ln P(I_p|B), & \text{if } f_p = \text{background label} \end{cases} \tag{8}$$

$$B_{p,q}(f_p, f_q) = \exp\left(-\frac{(I_p - I_q)^2}{2\sigma^2}\right) \cdot \frac{1}{d(p,q)} \cdot \delta(f_p, f_q) \tag{9}$$

$$\delta(f_p, f_q) = \begin{cases} 1, & \text{if } f_p \neq f_q \\ 0, & \text{otherwise} \end{cases} \tag{10}$$

where I_p is the intensity of pixel p; the *object label* is the label of the object (foreground); $P(I_p|O)$ and $P(I_p|B)$ are the probability of intensity of pixel p belonging to object and background, respectively, which are estimated from object and background intensity histograms during the training phase (details given below); $d(p,q)$ is the Euclidian distance between pixels p and q; and σ is the standard deviation of the intensity differences of neighboring voxels along the following boundary:

$$S_p(f_p) = 1 - \exp\left(-\frac{d(p, x_O)}{r_O}\right) \tag{11}$$

where $d(p, x_O)$ is the distance from pixel p to the set of pixels that constitute the interior of the current shape $\mathbf{x}_o$ of object O (note that if p is in the interior of $\mathbf{x}_o$, then $d(p, x_O) = 0$) and r_O is the radius of a circle that just encloses $\mathbf{x}_o$. The linear time method of [41] was used in this paper for computing this distance.

During the training stage, the histograms of intensity for each object are estimated from the training images. Based on this, $P(I_p|O)$ and $P(I_p|B)$ can be computed. As for parameters α, β, and γ in (9), since $\alpha+\beta+\gamma = 1$, we estimate only α and β by optimizing accuracy as a function of α and β and set $\gamma = 1-\alpha-\beta$. We use the gradient descent method for the optimization. Let $\mathrm{Accu}(\alpha, \beta)$ represent the algorithm's accuracy (here, we use the true positive volume fraction [44]), where α and β are initialized to 0.35 each; then, $\mathrm{Accu}(\alpha, \beta)$ is optimized over the training data set to determine the best α and β.

Minimizing EN with GCs: The minimization of (7) can be solved by the GC method. The graph is designed as follows. We take $V = P \cup L$, i.e., V contains all the pixel nodes and terminals corresponding to the labels in L, which represent objects of interest plus the background. $A = A_N \cup A_T$, where A_N is the n-links that connect pixels p and q ($p \in P, q \in N_p$) and with a weight of $\underline{w}_{p,q}$. A_T is the set of t-links, which connects pixel p and terminals $\ell \in L$ and with a weight of $\underline{w}_{p,\ell}$. The desired graph with cut cost $|C|$ equaling $\mathrm{En}(f)$ is constructed using the following weight assignments:

$$\underline{w}_{p,q} = \gamma \cdot B_{p,q} \tag{12}$$

$$\underline{w}_{p,\ell} = K - (\alpha \cdot D_p(\ell) + \beta \cdot S_p(\ell)) \tag{13}$$

where K is a constant that is large enough to make the weights $\underline{w}_{p,\ell}$ positive.

IGC–OAMM: We assume that the recognized shapes are sufficiently close to the actual boundaries in the given image to be

TABLE II
SLICE LOCALIZATION ERROR (IN MILLIMETERS) OF THE ORGAN TOP AND BOTTOM

Organ		Mean error (in mm) ± std.dev.
Liver	Top	5.1±2.5
	Bottom	9.2±5.1
Left kidney	Top	7.5±5.2
	Bottom	6.2±4.6
Right kidney	Top	8.3±6.5
	Bottom	7.1±5.8
Spleen	Top	8.1±5.2
	Bottom	7.3±6.1
Average		7.3±5.1

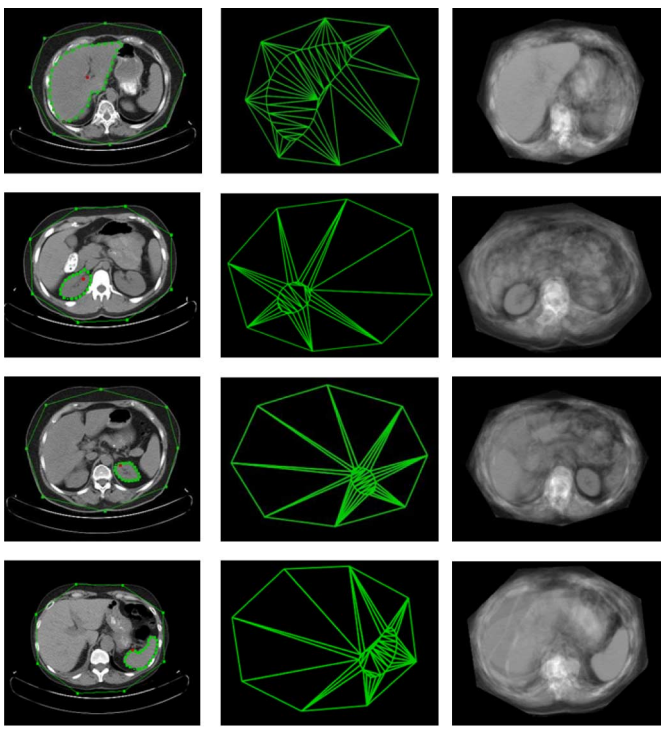

(a) (b) (c)

Fig. 6. Illustration of models used in organ initialization. The first, second, third and fourth rows correspond to liver, right kidney, left kidney, and spleen, respectively. (a) Landmarks of the organ and skin on one slice. (b) Corresponding AAM shape model for this slice level. (c) Corresponding AAM appearance model for this slice level.

TABLE III
NUMBER OF LANDMARKS AND SLICES USED IN MODELING

	Number of landmarks in organ	Number of landmarks in skin object	Number of interpolated slices
Liver	35	8	50
Left Kidney	20	8	32
Right Kidney	20	8	32
Spleen	26	8	32

segmented. The IGC–OAMM algorithm then determines what the new position of the landmarks of the objects represented in the initialized shape $\mathbf{x}_{\text{in}}$ should be such that the minimum GC cost is achieved, as presented in the following.

Algorithm 4: IGC–OAMM

Input: Initialized shapes $\mathbf{x}_{\text{in}}$, nIteration $= 3$.

Output: Resulting shapes $\mathbf{x}_{\text{out}}$ and the associated object boundaries.

Begin

For $i = 1 : \text{nIteration}$

1. Perform GC segmentation minimizing (7) based on the OAAM initialized shapes $\mathbf{x}_{\text{in}}$.
2. Compute the new position of the landmarks by moving each landmark in $\mathbf{x}_{\text{in}}$ to the point closest on the *GC* boundary; call the resulting shapes $\mathbf{x}_{\text{new}}$.
3. If no landmarks move, then set $\mathbf{x}_{\text{new}}$ as $\mathbf{x}_{\text{out}}$, and go to step 4.
   Else, subject $\mathbf{x}_{\text{new}}$ to the constraints of model $M_{3\text{D}}$, and call the result $\mathbf{x}_{\text{in}}$.

EndFor

4. Perform one final GC segmentation based on $\mathbf{x}_{\text{out}}$, and obtain the associated object boundaries.

End

In our implementation, we limit the distance that a landmark can move within any iteration to six voxels to make the change smoother.

III. EXPERIMENTAL RESULTS

The proposed methods were tested on a clinical CT data set. This data set contained images pertaining to 20 patients (ten male and ten female, ages 32 to 68), acquired from the precontrast phase of two different types of CT scanners (GE Medical systems, LightSpeed Ultra, and Philips, Mx8000 IDT 16). The pixel size varied from 0.55 to 1 mm, and slice thickness varied from 1 to 5 mm. Four experiments of liver, left kidney, right kidney, and spleen segmentation were conducted to evaluate the proposed method. Two investigators (XJ and UB) manually segmented all objects for the purpose of generating ground truth for evaluation. The leave-one-out strategy was used in the evaluation.

A. Evaluation of the Localization of the Top and Bottom Slices

The proposed slice localization method was used to detect the top and bottom slices of the liver, left kidney, right kidney, and spleen. These organs were manually checked to generate the reference standard of top and bottom positions. Table II shows the results. We observe that the localization of the top slice of liver is most accurate, which may be due to the high contrast in the lung region; whereas the localization of the bottom of liver has the largest error, which may be due to the lack of sufficient contrast in that region. The average localization error is 7.3 mm. Compared with Emrich et al's result [39] of 4.5 cm, the proposed method seems superior.

TABLE IV
MEAN AND STANDARD DEVIATION OF TPVF, FPVF FOR PSEUDO-3-D AAM, PSEUDO-3-D MAAM, 3-D MAAM, PSEUDO-3-D MOAAM, AND *IGC–OAMM* FOR LIVER, TWO KIDNEYS, AND SPLEEN WITH RESPECT TO REFERENCE SET 1

	TPVF (%)				FPVF (%)				Average Surface Dist (mm)			
	liver	left kidney	right kidney	spleen	liver	left kidney	right kidney	spleen	liver	left kidney	right kidney	spleen
Pseudo-3D AAM	60.0 ±5.1	51.0 ±8.4	53.0 ±6.4	59.3 ±7.3	10.12 ±2.38	15.36 ±3.25	12.15 ±3.01	14.62 ±4.35	12.12 ±5.32	11.59 ±4.39	10.98 ±4.78	11.32 ±4.12
Pseudo-3D MAAM	85.0 ±1.3	84.0 ±1.6	83.2 ±1.7	85.7 ±1.4	1.12 ±0.38	0.93 ±0.45	1.75 ±0.46	1.02 ±0.67	4.59 ±3.81	4.21 ±3.36	4.39 ±3.61	4.12 ±3.28
3D MAAM	90.5 ±0.9	90.2 ±1.0	90.4 ±1.5	91.3 ±0.9	0.46 ±0.11	0.55 ±0.12	0.59 ±0.13	0.67 ±0.16	2.01 ±1.21	1.82 ±1.06	1.72 ±0.98	1.61 ±0.88
Pseudo-3D MOAAM	90.1 ±1.1	89.3 ±1.2	89.5 ±1.6	90.7 ±1.5	0.53 ±0.05	0.67 ±0.06	0.62 ±0.11	0.71 ±0.13	1.93 ±1.03	1.62 ±0.92	1.81 ±1.25	1.73 ±1.03
Second rater	94.9 ±0.9	95.3 ±1.0	95.1 ±0.8	95.2 ±1.1	0.12 ±0.05	0.15 ±0.03	0.16 ±0.02	0.12 ±0.02	0.79 ±0.35	0.71 ±0.28	0.75 ±0.29	0.75 ±0.22
IGC-OAAM	94.0 ±0.9	94.2 ±1.1	94.4 ±0.9	94.7 ±1.4	0.16 ±0.03	0.13 ±0.02	0.21 ±0.03	0.15 ±0.02	0.81 ±0.32	0.75 ±0.25	0.79 ±0.33	0.76 ±0.29

B. Evaluation of Initialization

For helping with the initialization of liver, left and right kidneys, and spleen, the skin object is included in the model in addition to the object of interest. Fig. 6 shows an example slice and its corresponding mean shape and texture models for the four objects. We selected only eight landmarks for the skin object because LW works very well for this object even for such a small number of landmarks. We have validated manual landmarking by the equal-space labeling method. The correlation of the two methods is tested by a paired t-test, and the correlation is found to be 0.98. Table III summarizes the number of interpolated slices and the number of landmarks used in our experiments.

Results of a quantitative evaluation of the initialization approach are presented in Table IV. The accuracy in terms of true positive and false positive volume fractions (TPVF and FPVF) [44] is shown. TPVF indicates the fraction of the total amount of tissue in the true delineation; the FPVF denotes the amount of tissue falsely identified, which are defined as follows:

$$\text{TPVF} = \frac{|C_{\text{TP}}|}{|C_{\text{td}}|} \tag{14}$$

$$\text{FPVF} = \frac{|C_{\text{FP}}|}{|U_d - C_{\text{td}}|} \tag{15}$$

where U_d is assumed to be a binary scene with all voxels in the scene domain set to have a value 1, as shown in Fig. 7, and C_{td} is the set of voxels in the true delineation; $|\cdot|$ denotes volume. More details can be seen in [44]. The left column of Figs. 8 –11 shows the initialization results for the four objects.

Experiments were carried out to compare the performance of pseudo-3-D AAM (single object, slice-by-slice), pseudo-3-D MAAM (multiobject), real 3-D MAAM (multiobject), and the proposed pseudo-3-D MOAAM using reference set 1 as ground truth. We note that the multiobject strategy improves the accuracy considerably over a single-object AAM. The MOAAM method also improves the initialization performance due to the synergistic combination of the AAM and LW. The pseudo-3-D MOAAM and the real 3-D MAAM methods [42] have comparable performance; whereas the pseudo-3-D MOAAM method is about 12 times faster (see Table V). This is one of the reasons why we used the pseudo-3-D initialization method.

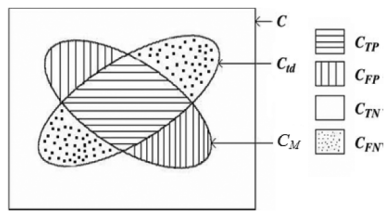

Fig. 7. Illustration of the accuracy factors for delineation for a binary case. Here, C denotes the whole scene, C_{td} denotes 'true' delineation, and C_M is the delineation result by method M.

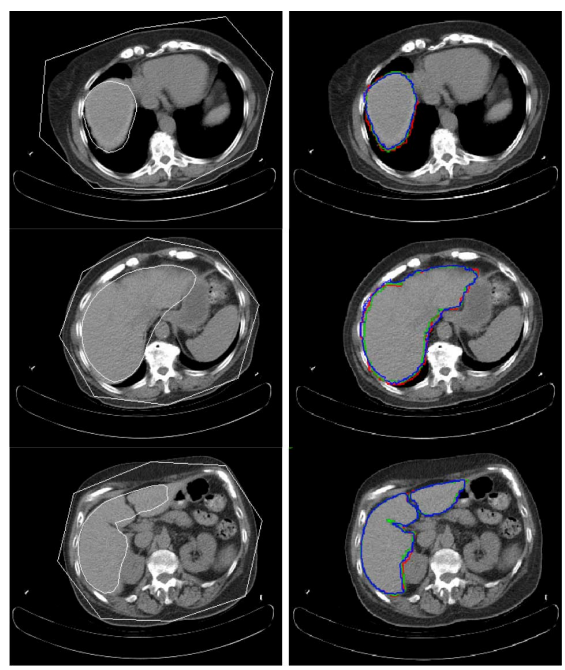

Fig. 8. Experimental results for three slice levels of liver segmentation. The left column is the MOAAM initialization result; the right is the IGC–OAMM result in which the red contour represents reference segmentation 1, green represents reference segmentation 2, and the blue contour represents segmentation by the proposed method.

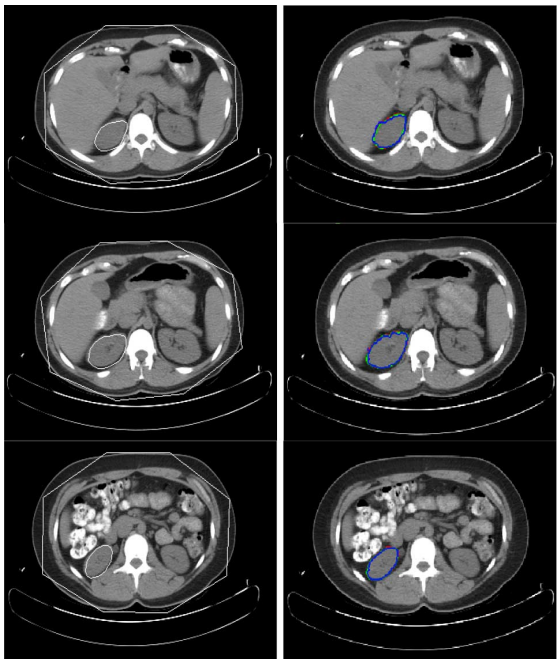

Fig. 9. Experimental results for three slice levels of right-kidney segmentation. The left column is the MOAAM initialization result; the right is the IGC–OAMM result in which the red contour represents reference segmentation 1, green represents reference segmentation 2, and the blue contour represents segmentation by the proposed method.

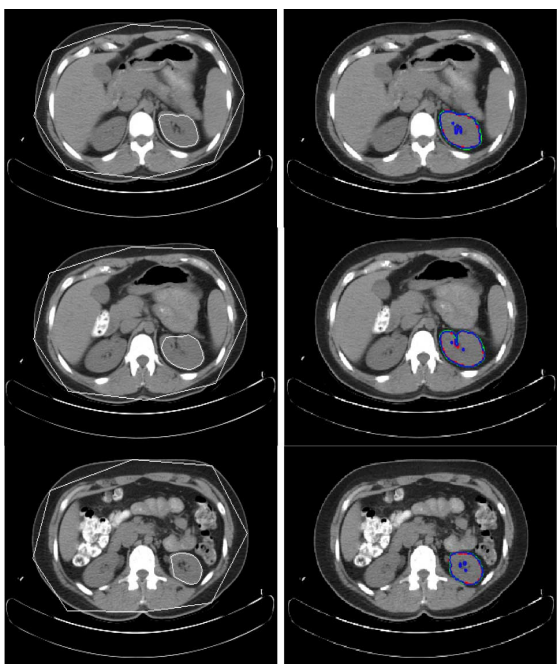

Fig. 10. Experimental results for three slice levels of left-kidney segmentation. The left column is the MOAAM initialization result; the right is the IGC–OAMM result in which the red contour represents reference segmentation 1, green represents Reference segmentation 2, and the blue contour represents segmentation by the proposed method.

After object recognition for all the slices, all the recognized shapes are stacked together to form a 3-D shape. Then, the method of refinement of shape proposed in Section II-C is applied if the 3-D shape is not transiting smoothly from slice to slice. We found that the OAAM recognition method works very well, and the refinement is called for only in very few cases.

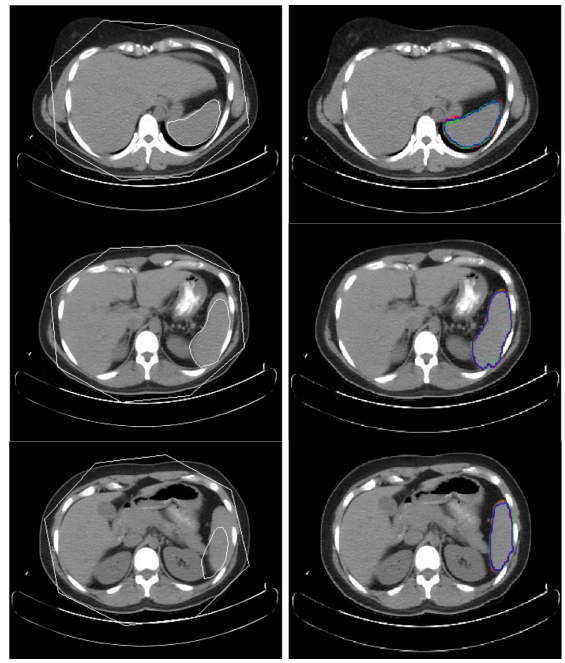

Fig. 11. Experimental results for three slice levels of spleen segmentation. The left column is the MOAAM initialization result; the right is the IGC–OAMM result in which the red contour represents reference segmentation 1, green represents reference segmentation 2, and the blue contour represents segmentation by the proposed method.

TABLE V
AVERAGE COMPUTATIONAL TIME (IN SECONDS) OVER ALL EXPERIMENTS FOR PSEUDO-3-D MAAM, 3-D MAAM, PSEUDO3-D MOAAM, AND IGC–OAMM

Organ	Average computational time (in seconds)			
	Pseudo-3D MAAM	*3D MAAM*	*Pseudo-3D MOAAM* (initialization)	*IGC-OAAM* (delineation)
Liver	50	732	60	310
Left Kidney	33	495	40	275
Right Kidney	32	476	40	260
Spleen	35	556	45	280

In a total of 80 (20×4) cases of organ recognition, there were seven cases with one slice of object recognition failed (liver:3, left kidney:1, right kidney:2, and spleen:1), and two cases with two slices failed (liver:1 and right kidney:1).

C. Evaluation of the IGC–OAMM Delineation Method

Evaluation on the Clinical Data Set: The accuracy of delineation by IGC–OAMM, expressed in TPVF, FPVF, and average symmetric surface distance [28], using reference set 1 is summarized in Table IV. A comparison of the reference segmentation 1 to the reference segmentation 2 is also shown in Table IV as a second rater. We observe that the average values of the TPVF and the FPVF are about 94.3% and 0.15%, respectively. In Figs. 8–11, the right column shows the IGC–OAMM segmentation results for the liver, left kidney, right kidney, and spleen. The mean distance, over all objects and the whole data set, between the segmented 3-D surface and the reference (true) surface was found to be 0.78 mm.

In terms of efficiency, Table V shows the computation time for the four objects on an Intel Xeon E5440 workstation with

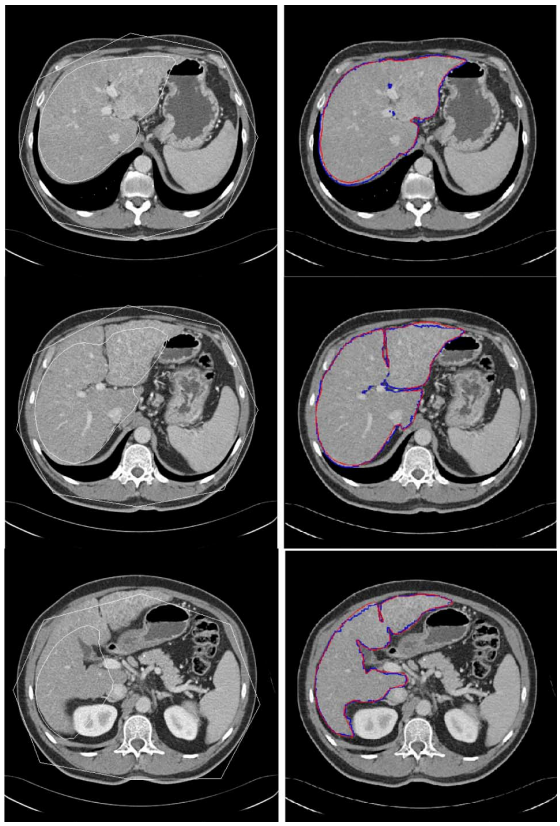

Fig. 12. Experimental results for three slice levels of one image in the MICCAI grand challenge data set. The left column is the MOAAM initialization result; the right is the IGC–OAMM result in which red contour represents the reference (ground truth) and blue contour represents segmentation by the proposed method.

TABLE VI
COMPARISON WITH OTHER METHODS ON THE MICCAI 2007 LIVER SEGMENTATION GRAND CHALLENGE DATA SET

Method	Runtime [min]	Overlap Error [%]	Volume difference [%]	Avg. distance [mm]	RMS distance [mm]	Max distance [mm]
Kainmüller et al.	15	6.1±2.1	-2.9±2.9	0.9±0.3	1.9±0.8	18.7±8.5
Heimann et al.	7	7.7±1.9	1.7±3.2	1.4±0.4	3.2±1.3	30.1±10.2
IGC-OAAM	6	6.5±1.8	-2.1±2.3	1.0±0.4	1.8±1.0	20.5±9.3

2.83-GHz CPU and 8 GB of RAM. The average total time (initialization + delineation) for segmenting one liver is about 310 s. Segmentation of kidney and spleen has similar computational time, which is about 270 s.

Evaluation on the MICCAI 2007 Grand Challenge Data Set: The proposed IGC–OAMM delineation method was also tested on the MICCAI 2007 Grand Challenge training data set using the leave-one-out strategy. There are 20 contrast-enhanced CT volumes of the abdomen in the training data set. All volumes have an in-plane resolution of 512×512 pixels and interslice spacing from 0.7 to 5.0 mm. Fig. 12 shows the recognition and delineation results for three slice levels of one image in this data set.

The proposed method was evaluated based on the "MICCAI 2007 Grand Challenge for liver segmentation" evaluation criteria [28]: volumetric overlap error, volume difference, symmetric average surface distance, symmetric RMS surface distance, and maximal surface distance. The results achieved by the proposed method and by previous work from the literature are summarized in Table VI. Compared with the best performance (Kainmüller *et al.* [29]), our method has comparable performance but runs much faster (6 versus 15 min).

IV. CONCLUSION AND DISCUSSIONS

In this paper, we have proposed a 3-D automatic anatomy segmentation method. The method effectively combines the AAM, LW, and GC ideas to exploit their complementary strengths. It consists of three main parts: model building, initialization, and delineation. For the initialization (recognition) part, we employ a pseudo-3-D strategy and segment the organs slice by slice via the MOAAM method, which synergistically combines the AAM and LW methods. For the delineation part, an iterative GC–OAMM method is proposed, which integrates the shape information gathered from initialization with a GC algorithm. The method was tested on a clinical CT data set from 20 patients for segmenting the liver, kidneys, and spleen. The experimental results suggested that an overall segmentation accuracy of TPVF $> 94.3\%$ and FPVF $< 0.2\%$ can be achieved.

For initialization, we employed a pseudo-3-D strategy and combined AAM and LW methods to improve the performance. The multiobject strategy also helped initialization due to increased constraints. Compared with the real 3-D AAM method, the pseudo-3-D OAAM approach has comparable accuracy while achieving roughly a 12-fold speed up. The purpose of initialization is to provide a rough object localization and shape constraints for a latter GC method, which will produce refined delineation. We suggest that it is better to have a fast and robust method than a slow and more accurate technique for initialization.

For delineation, the shape-constrained GC method is the core part of the whole system. Several similar ideas were also proposed in the literature [33]–[37]. However, they are mostly tested on 2-D images, and it is difficult to compare with these methods because the testing data sets used are different.

In Figs. 8–11 and from the results in Table VI, the proposed method appears to slightly undersegment the organs. This may be due to two reasons. First, the shape term designed in our cost function is not symmetric. We did not put penalty on the pixel if it is inside the shape. That is because we find that there are usually some pixels not belonging to the target organ but still inside the shape, such as urine inside the kidney (see Fig. 10). Our method can exclude such pixels. This is one of the strengths of our method. Second, as per our experience, experts tend to oversegment the organ during the process of manually delineating the boundaries due to illumination of the room, tiredness, changing window parameters, and poor image qualities. This is rather a general problem reported by many researchers.

Although localizing a CT slice within a human body can greatly facilitate the workflow of a physician, so far, this area of research has not received much attention. The proposed slice localization method aims to localize the top and bottom slices of organs automatically, which is an important part of the whole system. The average localization error over the whole data set and all organs is about 7.3 mm, which seems accurate enough

for clinical use. In a similar manner, it can also be used to localize any slice by constructing the corresponding slice model.

In this paper, only one object has been delineated at a time. With the shape constraints of multiple organs, the proposed IGC–OAMM method can be easily generalized to segment multiple organs simultaneously. However, this brings up an issue for GC, i.e., the unavailability of a globally optimal min cut solution for simultaneously segmenting multiple objects. For single-object segmentation, global optimality is guaranteed. For multiple objects, the α-expansion method can find segmentations only within a known factor of the global optimum [45].

The proposed method takes about 5 min for segmenting one organ. To make it more practical in clinical applications, the parallelization or multithread implementation of the algorithm is one potential solution. Anderson et al. [47] and Liu et al. [48] proposed parallelization of the GC methods and achieved good performance. The parallelization of the proposed method will be investigated in the near future.

An executable version of our implementation of the 3-D shape-constrained GC method with a user interface can be downloaded from http://xinjianchen.wordpress.com/research/.

ACKNOWLEDGMENT

We would like to thanks Dr. Drew A. Torigian from University of Pennsylvania, Philadelphia, for providing the data.

REFERENCES

[1] L. Ruskó, G. Bekes, G. Németh, and M. Fidrich, "Fully automatic liver segmentation for contrast-enhanced CT images," in *Proc. MICCAI Workshop 3-D Segment. Clinic, Grand Challenge*, 2007, pp. 143–150.

[2] T. Kaneko, L. Gu, and H. Fujimoto, "Recognition of abdominal organs using 3D mathematical morphology," *Syst. Comput. Jpn.*, vol. 33, no. 8, pp. 75–83, 2002.

[3] M. Kass, A. Witkin, and D. Terzopoulos, "Snakes: Active contour models," *Int. J. Comput. Vis.*, vol. 1, no. 4, pp. 321–331, Jan. 1988.

[4] F. Liu, B. Zhao, P. K. Kijewski, L. Wang, and L. H. Schwartz, "Liver segmentation for CT images using GVF snake," *Med. Phys.*, vol. 32, no. 12, pp. 3699–3706, Dec. 2005.

[5] R. Malladi, J. A. Sethian, and B. C. Vemuri, "Shape modeling with front propagation: A level set approach," *IEEE Trans. Pattern Anal. Mach. Intell.*, vol. 17, no. 2, pp. 158–175, Feb. 1995.

[6] A. X. Falcao, J. K. Udupa, S. Samarasekera, and S. Sharma, "User-steered image segmentation paradigms: Live wire and live lane," *Graph. Models Image Process.*, vol. 60, no. 4, pp. 233–260, Jul. 1998.

[7] V. Grau, A. U. J. Mewes, M. Alcañiz, R. Kikinis, and S. K. Warfield, "Improved watershed transform for medical image segmentation using prior information," *IEEE Trans. Med. Imag.*, vol. 23, no. 4, pp. 447–458, Apr. 2004.

[8] J. K. Udupa and S. Samarasekera, "Fuzzy connectedness and object definition: Theory, algorithms, and applications in image segmentation," *Graph. Models Image Process.*, vol. 58, no. 3, pp. 246–261, May 1996.

[9] J. K. Udupa, P. K. Saha, and R. A. Lotufo, "Relative fuzzy connectedness and object definition: Theory, algorithms, and applications in image segmentation," *IEEE Trans. Pattern Anal. Mach. Intell.*, vol. 24, no. 11, pp. 1485–1500, Nov. 2002.

[10] Y. Boykov and V. Kolmogorov, "An experimental comparison of min-cut/max-flow algorithms," *IEEE Trans. Pattern Anal. Mach. Intell.*, vol. 26, no. 9, pp. 1124–1137, Sep. 2004.

[11] V. Kolmogorov and R. Zabih, "What energy functions can be minimized via graph cuts?," *IEEE Trans. Pattern Anal. Mach. Intell.*, vol. 26, no. 2, pp. 147–159, Feb. 2004.

[12] A. Besbes, N. Komodakis, G. Langs, and N. Paragios, "Shape priors and discrete MRFs for knowledge-based segmentation," in *Proc. IEEE Comput. Soc. Conf. Comput. Vis. Pattern Recogn.*, 2009, pp. 1295–1302.

[13] H. Park, P. Bland, and C. Meyer, "Construction of an abdominal probabilistic atlas and its application in segmentation," *IEEE Trans. Med. Imag.*, vol. 22, no. 4, pp. 483–492, Apr. 2003.

[14] M. B. Cuadra, C. Pollo, A. Bardera, O. Cuisenaire, J.-G. Villemure, and J.-P. Thiran, "Atlas-based segmentation of pathological MR brain images using a model of lesion growth," *IEEE Trans. Med. Imag.*, vol. 23, no. 10, pp. 1301–1314, Oct. 2004.

[15] P. L. Basin and D. L. Pham, "Homeomorphic brain image segmentation with topological and statistical atlases," *Med. Image Anal.*, vol. 12, no. 5, pp. 616–625, Oct. 2008.

[16] J. H. Noble and B. M. Dawant, "Automatic segmentation of the optic nerves and chiasm in CT and MR using the atlas-navigated optimal medial axis and deformable-model algorithm," in *Proc. SPIE*, 2009, vol. 7259, pp. 725 916-1–725 916-10.

[17] X. Zhou, T. Hayashi, M. Han, H. Chen, T. Hara, H. Fujita, R. Yokoyama, M. Kanematsu, and H. Hoshi, "Automated segmentation and recognition of the bone structure in non-contrast torso CT images using implicit anatomical knowledge," in *Proc. SPIE*, 2009, vol. 7259, pp. 72 583-4–72 593S-1.

[18] A. F. Frangi, D. Rueckert, J. A. Schnabel, and W. J. Niessen, "Automatic construction of multiple-object three-dimensional statistical shape models: Application to cardiac modeling," *IEEE Trans. Med. Imag.*, vol. 21, no. 9, pp. 1151–1166, Sep. 2002.

[19] S. Seifert, A. Barbu, S. K. Zhou, D. Liu, J. Feulner, M. Huber, M. Suehling, A. Cavallaro, and D. Comaniciu, "Hierarchical parsing and semantic navigation of full body CT data," in *Proc. SPIE*, 2009, vol. 7259, pp. 725 902-1–725 902-8.

[20] H. Ling, S. K. Zhou, Y. Zheng, B. Georgescu, M. Suehling, and D. Comaniciu, "Hierarchical, learning-based automatic liver segmentation," in *Proc. IEEE Comput. Soc. Conf. Comput. Vis. Pattern Recogn.*, 2008, pp. 1–8.

[21] S. C. Mitchell, B. P. F. Lelieveldt, R. J. van der Geest, H. G. Bosch, J. H. C. Reiber, and M. Sonka, "Multistage hybrid active appearance model matching: Segmentation of left and right ventricles in cardiac MR images," *IEEE Trans. Med. Imag.*, vol. 20, no. 5, pp. 415–423, May 2001.

[22] T. McInerney and D. Terzopoulos*, Deformable Models, Handbook of Medical Imaging: Processing and Analysis*, I. Bankman, Ed. New York: Academic, 2000.

[23] X. Artaechevarria, A. Muñoz-Barrutia, and C. Ortiz-de-Solórzano, "Combination strategies in multi-atlas image segmentation: Application to brain MR data," *IEEE Trans. Med. Imag.*, vol. 28, no. 8, pp. 1266–1277, Aug. 2009.

[24] G. Christensen, R. Rabbitt, and M. Miller, "3-D brain mapping using a deformable neuroanatomy," *Phys. Med. Biol.*, vol. 39, pp. 609–618, 1994.

[25] T. F. Cootes, C. J. Taylor, D. H. Cooper, and J. Graham, "Active shape models—Their training and application," *Comput. Vis. Image Underst.*, vol. 61, no. 1, pp. 38–59, Jan. 1995.

[26] T. F. Cootes, G. Edwards, and C. Taylor, "Active appearance models," *IEEE Trans. Pattern Anal. Mach. Intell.*, vol. 23, no. 6, pp. 681–685, Jun. 2001.

[27] M. B. Stegmann, B. K. Ersbll, and R. Larsen, "FAME—A flexible appearance modelling environment," *IEEE Trans. Med. Imag.*, vol. 22, no. 10, pp. 1319–1331, Oct. 2003.

[28] T. Heimann, B. Ginneken, M. A. Styner, Y. Arzhaeva, V. Aurich, C. Bauer, A. Beck, C. Becker, R. Beichel, G. Bekes, F. Bello, G. Binnig, H. Bischof, A. Bornik, P. Cashman, A. Cordova, B. M. Dawant, M. Fidrich, J. D. Furst, D. Furukawa, L. Grenacher, J. Hornegger, D. Kainmuller, R. I. Kitney, H. Kobatake, H. Lamecker, T. Lange, B. Lennon, H.-P. Meinzer, G. Nemeth, D. S. Raicu, A.-M. Rau, E. M. van Rikxoort, M. Rousson, L. Rusko, K. A. Saddi, G. Schmidt, D. Seghers, A. Shimizu, P. Slagmolen, E. Sorantin, G. Soza, R. Susomboon, J. M. Waite, A. Wimmer, and I. Wolf, "Comparison and evaluation of methods for liver segmentation from CT datasets," *IEEE Trans. Med. Imag.*, vol. 28, no. 8, pp. 1251–1265, Aug. 2009.

[29] D. Kainmüller, T. Lange, and H. Lamecker, "Shape constrained automatic segmentation of the liver based on a heuristic intensity model," in *Proc. MICCAI Workshop 3-D Segment. Clinic, Grand Challenge*, 2007, pp. 109–116.

[30] J. M. Liu and J. K. Udupa, "Oriented active shape models," *IEEE Trans. Med. Imag.*, vol. 28, no. 4, pp. 571–584, Apr. 2009.

[31] K. Haris, S. N. Efstratiadis, N. Maglaveras, and A. K. Katsaggelos, "Hybrid image segmentation using watersheds and fast region merging," *IEEE Trans. Image Process.*, vol. 7, no. 12, pp. 1684–1699, Dec. 1998.

[32] J. Yang and J. S. Duncan, "3D image segmentation of deformable objects with joint shape-intensity prior models using level sets," *Med. Image Anal.*, vol. 8, no. 3, pp. 285–294, Sep. 2004.
[33] D. Freedman and T. Zhang, "Interactive graph cut based segmentation with shape priors," in *Proc. IEEE Comput. Soc. Conf. Comput. Vis. Pattern Recogn.*, 2005, pp. 755–762.
[34] A. Ayvaci and D. Freedman, "Joint segmentation-registration of organs using geometric models," in *Proc. IEEE Eng. Med. Biol. Soc.*, 2007, pp. 5251–5254.
[35] M. Kumar, P. Torr, and A. Zisserman, "ObjCut," in *Proc. IEEE Comput. Society Conference on Computer Vision and Pattern Recognition*, 2005, pp. 18–23.
[36] J. J. Malcolm, Y. Y. Rathi, and A. A. Tannenbaum, "Graph cut segmentation with nonlinear shape priors," in *Proc. IEEE Int. Conf. Image Process.*, 2007, vol. IV, pp. 365–368.
[37] N. Vu and B. S. Manjunath, "Shape prior segmentation of multiple objects with graph cuts," in *Proc. IEEE Comput. Soc. Conf. Comput. Vis. Pattern Recogn.*, 2008, pp. 1–8.
[38] B. Haas, T. Coradi, M. Scholz, P. Kunz, M. Huber, U. Oppitz, L. André, V. Lengkeek, D. Huyskens, A. van Esch, and R. Reddick, "Automatic segmentation of thoracic and pelvic CT images for radiotherapy planning using implicit anatomic knowledge and organ-specific segmentation strategies," *Phys. Med. Biol.*, vol. 53, no. 6, pp. 1751–1771, Mar. 2008.
[39] T. Emrich, F. Graf, H. P. Kriegel, M. Schubert, M. Thoma, and A. Cavallaro, "CT slice localization via instance-based regression," in *Proc. SPIE*, 2010, vol. 7623, pp. 762 320-1–762 320-12.
[40] C. Brechbuhler, G. Gerig, and O. Kubler, "Parameterization of closed surfaces for 3D shape description," *Comput. Vis. Image Underst.*, vol. 62, no. 2, pp. 154–170, 1995.
[41] C. R. Maurer, Jr., R. S. Qi, and V. Raghavan, "A linear time algorithm for computing exact Euclidean distance transforms of binary images in arbitrary dimensions," *IEEE Trans. Pattern Anal. Mach. Intell.*, vol. 25, no. 2, pp. 265–270, Feb. 2003.
[42] S. C. Mitchell, J. G. Bosch, B. P. F. Lelieveldt, R. J. van der Geest, J. H. C. Reiber, and M. Sonka, "3-D active appearance models: Segmentation of cardiac MR and ultrasound images," *IEEE Trans. Med. Imag.*, vol. 21, no. 9, pp. 1167–1178, Sep. 2002.
[43] X. Chen, J. K. Udupa, A. Alavi, and D. A. Torigian, "Automatic anatomy recognition via multiobject oriented active shape models," *Med. Phys.*, vol. 37, no. 12, pp. 6390–6401, Dec. 2010.
[44] J. K. Udupa, V. R. Leblanc, Y. Zhuge, C. Imielinska, H. Schmidt, L. M. Currie, B. E. Hirsch, and J. Woodburn, "A framework for evaluating image segmentation algorithms," *Comput. Med. Imag. Graph.*, vol. 30, no. 2, pp. 75–87, Mar. 2006.
[45] Y. Boykov, O. Veksler, and R. Zabih, "Fast approximate energy minimization via graph cuts," *IEEE Trans. Pattern Anal. Mach. Intell.*, vol. 23, no. 11, pp. 1222–1239, Nov. 2001.
[46] O. Veksler, "Star-shape prior for graph-cut image segmentation," in *Proc. 10th Eur. Conf. Comput. Vis.*, 2008, pp. 454–467.
[47] R. Anderson and J. Setubal, "A parallel implementation of the push-relabel algorithm for the maximum flow problem," *J. Parallel Distrib. Comput.*, vol. 29, no. 1, pp. 17–26, Aug. 1995.
[48] J. Liu and J. Sun, "Parallel graph-cuts by adaptive bottom-up merging," in *Proc. IEEE Comput. Soc. Conf. Comput. Vis. Pattern Recogn.*, 2010, pp. 2181–2188.
[49] I. Dryden and K. V. Mardia, *Statistical Shape Analysis*. Hoboken, NJ: Wiley, 1998, 10: 0471958166.

Xinjian Chen received the Ph.D. degree from the Institute of Automation, Chinese Academy of Sciences, Beijing, China, in 2006.

After graduation, he entered Microsoft Research Asia and researched on handwriting recognition. From January 2008 to October 2009, he was a Postdoctoral Fellow with the Medical Image Processing Group, Department of Radiology, University of Pennsylvania, Philadelphia. From October 2009, he has been a Postdoctoral Fellow with the Deparment of Radiology and the Image Sciences, Clinical Center, National Institutes of Health, Bethesda, MD. His research interests include medical image processing, pattern recognition, machine learning, and their applications.

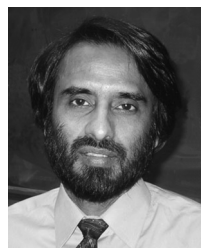

Jayaram K. Udupa received the Ph.D. degree in computer science from the Indian Institute of Science, Bangalore, India, in 1976, with a medal for best Ph.D. research.

Since 1981, he has been with the University of Pennsylvania, Philadelphia, where since 1994, he has been a Professor of radiological science and, since 1991, the Chief of the Medical Image Processing Group. He is an author of two edited books, 165 journal papers, and 170 full conference papers, and has given 260 invited talks worldwide. He has offered consultancy to several imaging companies in their early stages, organized early conferences and workshops in medical image processing and visualization, and developed and distributed large software systems for medical 3-D imaging. His current research interests include building bodywide fuzzy models toward making the practice of clinical radiology quantitative.

Dr. Udupa is a Fellow of the Institute of Electrical and Electronic Engineers and the American Institute of Medical and Biological Engineering.

Ulas Bagci received the B.Sc. in electrical and electronics engineering from Bilkent University, Ankara, Turkey, in 2003; the M.Sc. degrees in electrical and electronics engineering from Koc Universities, Istanbul, Turkey, in 2005; and the Ph.D. degree in computer science, University of Nottingham, Nottingham, U.K., in 2010.

He was a visiting Research Fellow with the Department of Radiology, University of Pennsylvania, Philadelphia, in 2009. Since 2010, he has been an ISTP Research Fellow with the Center for Infectious Disease Imaging, National Institutes of Health, Bethesda, MD. His current research interests include statistical and computational models of functional and anatomical images, and clinical image processing and analysis.

Dr. Bagci was the recipient of several awards including EU Marie Curie Fellowship (2006–2009) and NIH-FARE (2012).

Ying Zhuge received the Ph.D. degree in computer science from the Institute of Automation, Chinese Academy of Sciences, Beijing, China, in 1999.

He was a Research Associate with the Medical Image Processing Group, Department of Radiology, University of Pennsylvania, Philadelphia. Then, he was a Senior Computer Scientist with the Naviscan PET system, Inc. He is currently a Computer Scientist with the Radiation Oncology Branch, National Cancer Institute, National Institutes of Health, Bethesda, MD. His research interests include pattern recognition, medical image processing, and their biomedical applications.

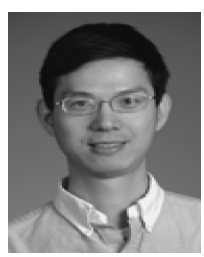

Jianhua Yao received B.S. degree in computer science from Tianjin University, TianjinChina; the M.S. degrees in computer science from Tsinghua University, BeijingChina; and the Ph.D. degree in computer science from Johns Hopkins University, Baltimore, MD.

Since 2002, he has been with the National Institutes of Health (NIH), Bethesda, MD, as a Staff Scientist, where he directs a clinical image processing laboratory. He is also affiliated with the Imaging Biomarker and Computer-Aided Diagnosis Laboratory, NIH. He is the author of 150 papers in journals and conference proceedings and is the holder of two patents in colon-cancer CAD technique. His research interests include clinical image processing, deformable model, nonrigid registration, CAD, and CT colonography.